Cell Reports
Physical Science

CellPress
OPEN ACCESS

Article

A spontaneously formed plasmonic-$MoTe_2$ hybrid platform for ultrasensitive Raman enhancement

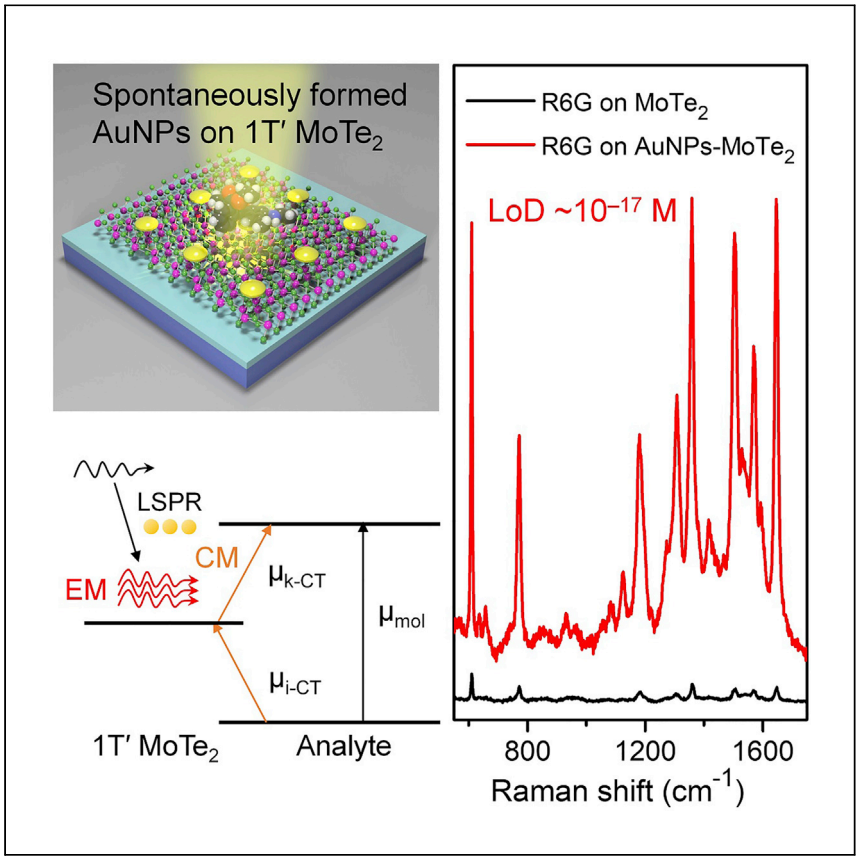

A spontaneously fabricated hybrid structure consisting of 2D 1T′ $MoTe_2$ and gold nanoparticles for ultrasensitive SERS detection is reported by Tao et al. The hybrid structure generates coupled electromagnetic and chemical enhancements, rendering a superior limit of detection at 10^{-17} M, and the SERS signals are uniform, reproducible, stable, and clean.

Li Tao, Zhiyong Li, Kun Chen, ..., Teng Qiu, Xi Wan, Jian-Bin Xu

taoli@link.cuhk.edu.hk (L.T.)
chenk69@mail.sysu.edu.cn (K.C.)
jbxu@ee.cuhk.edu.hk (J.-B.X.)

Highlights

Plasmonic-$MoTe_2$ hybrid structure is spontaneously fabricated

The 1T′ phase of $MoTe_2$ is essential for plasmonic nanoparticle formation

The hybrid platform generates strong EM-CM coupling for ultrasensitive SERS

Flexible SERS tapes show promise in practical applications

Tao et al., Cell Reports Physical Science 2, 100526
August 18, 2021
https://doi.org/10.1016/j.xcrp.2021.100526

Cell Reports
Physical Science

CellPress
OPEN ACCESS

Article

A spontaneously formed plasmonic-$MoTe_2$ hybrid platform for ultrasensitive Raman enhancement

Li Tao,[1,2,8,*] Zhiyong Li,[1] Kun Chen,[3,*] Yaoqiang Zhou,[1] Hao Li,[1] Ximiao Wang,[3] Runze Zhan,[3] Xiangyu Hou,[4] Yu Zhao,[5] Junling Xu,[6] Teng Qiu,[4] Xi Wan,[7] and Jian-Bin Xu[1,*]

SUMMARY

Development of highly sensitive, stable, and repeatable surface-enhanced Raman scattering (SERS) substrates is crucial for analytical detection, which is a challenge for traditional metallic structures. Here, by exploiting the high surface activity of the 1T′ transition metal telluride, we fabricate high-density gold nanoparticles (AuNPs) that are prepared spontaneously *in situ* on the 1T′ $MoTe_2$ atomic layers, forming a plasmonic-2D material hybrid SERS substrate. This AuNP formation is unique to the 1T′ phase, which is repressed in 2H $MoTe_2$ with lower surface activity. The hybrid structure generates coupling effects of electromagnetic and chemical enhancements, as well as excellent molecule adsorption, leading to ultrasensitive (4×10^{-17} M) and reproducible detection. Flexible SERS tapes are demonstrated in practical applications. Our approach facilitates ultrasensitive SERS detection by a facile method, as well as an enhanced mechanistic understanding of SERS beyond plasmonic effects.

INTRODUCTION

Surface-enhanced Raman scattering (SERS) has been investigated intensively as a promising analytical tool for non-destructive and label-free fingerprint molecular detection.[1] Metallic plasmonic nanostructures are widely studied as sensitive SERS platforms because of the largely augmented electromagnetic field generated by localized surface plasmon resonance (LSPR) at hotspots, known as the electromagnetic mechanism (EM).[2] However, the noble metal structures for SERS suffer from significant limitations, including (1) a complicated and delicate fabrication process with design constraints, (2) low reproducibility and uniformity, (3) large analyte fluorescence (FL) backgrounds, and (4) metal-catalyzed side reactions and photobleaching effect.[3] In recent years, graphene and other 2D layered materials have drawn great attention as new types of SERS substrates.[4–7] The atomic flat 2D materials uniformly adsorb the analytes, forming strongly interacting interfaces. In contrast with the plasmonic structures, the SERS effect on 2D material substrates relies on the chemical mechanism (CM) that stems from the photo-induced charge transfer in the analyte-2D material interface.[8–10] The CM-based 2D material substrates show advantages over the noble metal SERS structures in terms of stability, reproducibility, quenched FL signals, etc. Recently we reported novel 1T′ transition metal telluride (TMT) atomic layers as ultrasensitive CM-based SERS platforms.[11] The semi-metallic tellurides generate strong coupling with the adsorbed molecules and provide a high density of states for the charge transfer, delivering much better SERS performance over graphene. Other semi-metallic 2D materials with abundant low-energy states, such as NbS_2 and ReO_xS_y, have been demonstrated to exhibit superior SERS sensitivities.[12,13]

[1]Department of Electronic Engineering, The Chinese University of Hong Kong, Hong Kong SAR, China

[2]Key Lab of Advanced Optoelectronic Quantum Architecture and Measurement (Ministry of Education), School of Physics, Beijing Institute of Technology, Beijing 100081, China

[3]State Key Laboratory of Optoelectronic Materials and Technologies, School of Electronics and Information Technology and Guangdong Province Key Laboratory of Display Material, Sun Yat-sen University, Guangzhou 510275, China

[4]School of Physics, Southeast University, Nanjing 211189, China

[5]Guangdong Provincial Key Laboratory of Functional Soft Condensed Matter, School of Material and Energy, Guangdong University of Technology, Guangzhou 510006, China

[6]Institute of Textiles and Clothing, The Hong Kong Polytechnic University, Hong Kong SAR, China

[7]Department of Electronic Engineering, Jiangnan University, Wuxi 214122, China

[8]Lead contact

*Correspondence: taoli@link.cuhk.edu.hk (L.T.), chenk69@mail.sysu.edu.cn (K.C.), jbxu@ee.cuhk.edu.hk (J.-B.X.)

https://doi.org/10.1016/j.xcrp.2021.100526

Hybrid SERS platforms consisting of plasmonic structures and 2D materials are proposed to be promising candidates for next-generation molecular sensors because they allow a combination of advantages of EM and CM.[14] Previous studies have shown that 2D graphene and hexagonal boron nitride (*h*BN) films hybridized with thermally deposited noble metal nanoparticles can efficiently enhance SERS sensitivity and partly solve the abovementioned challenging issues of noble metals.[15–21] The 2D materials serve as a shield for noble metals, provide additional chemical enhancement, and reduce the molecular FL. However, chemical enhancement of graphene and *h*BN is limited, and thermal deposition of noble metal nanoparticles involves additional costly fabrication processes. In addition, depositing noble metal nanoparticles on 2D materials causes potential damage to the 2D materials,[22] and covering pre-deposited noble metal nanoparticles with 2D materials introduces interface quality degradation during the transfer processes.

2D TMT can effectively enrich the adsorbed probe molecules and generate significant chemical enhancement. More importantly, the low-symmetry atomic structure of 1T′ TMT makes its surface highly active, which ensures a strongly interacting analyte-TMT interface, leading to coupled electromagnetic and chemical enhancements for SERS in the plasmonic-TMT hybrid structure. In the present study, we report facile and high-throughput fabrication of the hybrid structure of $MoTe_2$ atomic layers and gold nanoparticles (AuNPs) as a high-performance SERS mediator. In contrast with thermal deposition, the uniformly distributed AuNPs are fabricated spontaneously *in situ* on the $MoTe_2$ surface by a redox reaction with the gold precursor. The unique large surface activity of the 1T′-phase $MoTe_2$ plays a key role in formation of AuNPs, as evidenced by comparative investigation of $MoTe_2$ with different phases. The plasmonic-$MoTe_2$ hybrid structure exhibits an ultralow detection limit of 4×10^{-17} M for the Rhodamine 6G (R6G) probe, which is four orders of magnitude improved in comparison with the individual $MoTe_2$, and the SERS signals are reproducible, stable, uniform, and clean. Practical application, including food safety control, is demonstrated in the AuNPs-$MoTe_2$ platform, showing great potential for highly sensitive and reliable SERS detection.

RESULTS

Fabrication of the plasmonic-$MoTe_2$ hybrid platform

Large-scale and highly crystalline trilayer (3L) $MoTe_2$ samples synthesized by salt-assisted chemical vapor deposition (CVD) method were adopted for the experiments, as shown in Figure 1A. The highly crystalline and atomic flat features of the as-grown 1T′ $MoTe_2$ were confirmed by Raman spectroscopy, atomic force microscopy (AFM), and high-resolution transmission electron microscopy (HRTEM) (Figure S1). *In situ* formation of AuNPs on 1T′ $MoTe_2$ atomic layers was realized by simply immersing the sample in $HAuCl_4$ solution in ethanol (1 mM) for 30 s (Figure 1B), followed by gentle drying with nitrogen flow. Scanning electron microscopy (SEM) images of 1T′ $MoTe_2$ before and after treatment (Figures 1C and 1D) reveal the dense and uniform morphology of AuNPs decorated on the $MoTe_2$ surface with diameters of ~20 nm. Importantly, the AuNPs were found exclusively on $MoTe_2$, whereas the SiO_2 regions remained intact. 2D 1T′ $MoTe_2$ has considerable surface activity associated with the distorted octahedral lattice, leading to spontaneous *in situ* transition from $[AuCl_4]^-$ into AuNPs in the $HAuCl_4$ solution without an additional reduction agent.[23,24] In contrast, reduction agents such as trisodium citrate or pretreatments such as laser processing are required for growing AuNPs on other less active 2D materials, such as graphene and MoS_2, in most synthetic strategies.[25–27] The atomic structure of the AuNPs-$MoTe_2$ hybrid was investigated by HRTEM, as shown in Figure 1E. $MoTe_2$ at the nanogaps between the AuNPs exhibited an

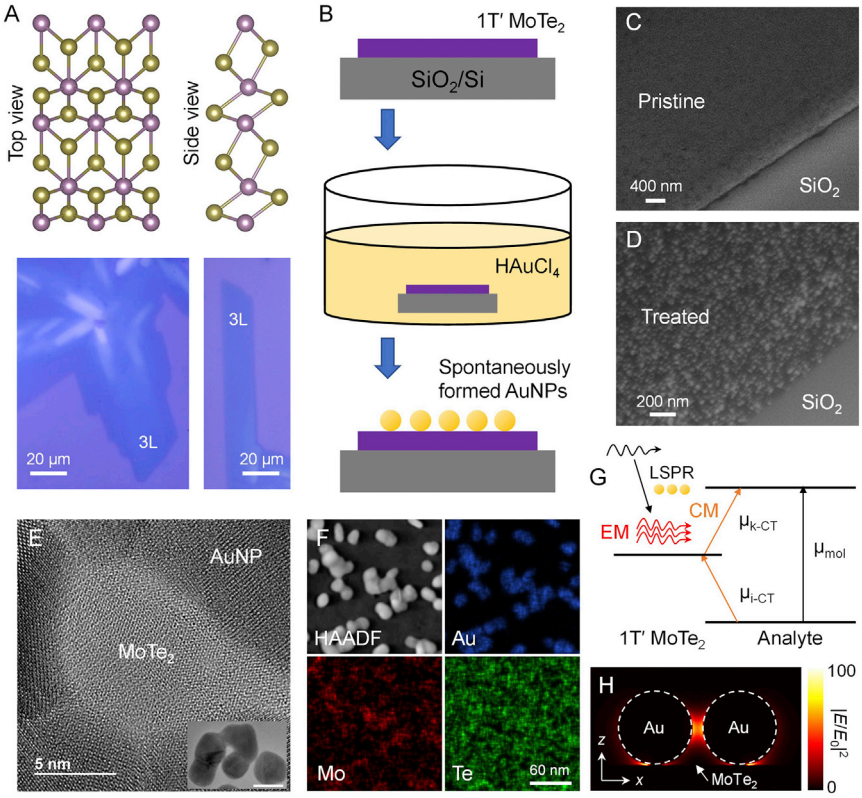

Figure 1. Spontaneous formation of AuNPs on 1T′ $MoTe_2$ for SERS with EM-CM coupling

(A) Lattice structure and optical images of 1T′ $MoTe_2$ atomic layers.

(B) Schematic of spontaneous *in situ* formation of AuNPs on the surface of 1T′ $MoTe_2$.

(C and D) SEM images of 1T′ $MoTe_2$ before and after decoration of AuNPs.

(E) HRTEM image of the AuNPs-$MoTe_2$ structure. Inset: a lower-magnification image. Scale bar in the inset, 20 nm.

(F) HAADF image and the corresponding elemental maps of the AuNPs-$MoTe_2$ structure.

(G) Illustration showing the coupling of EM and CM in the AuNPs-$MoTe_2$ hybrid SERS structure.

(H) Simulated electrical field distribution of the AuNPs-$MoTe_2$ structure (front view). Diameter of the AuNPs, 20 nm; gap between the AuNPs, 3 nm.

excellent 1T′ octahedral lattice, indicating that the $MoTe_2$ was well preserved after $HAuCl_4$ treatment. Additional TEM images are available in Figure S2A and S2B. Figure 1F shows a high-angle annular dark field (HAADF) image of AuNPs-$MoTe_2$ and elemental maps collected by energy-dispersive X-ray spectrometer. The Au map fits well with the bright areas in the HAADF image, whereas the uniformly distributed Mo and Te elements reveal the intact $MoTe_2$ film underneath. X-ray photoelectron spectroscopy (XPS) investigation of the $MoTe_2$ flake shown in Figures S2C–S2G revealed the emergence of Au $4f_{5/2}$ and Au $4f_{7/2}$ peaks derived from the AuNPs after $HAuCl_4$ treatment, whereas the positions and shapes of Te 3d and Mo 3d peaks were unchanged after treatment.

Coupling of EM and CM in the hybrid platform

The metallic plasmonic structure creates hotspots where significantly enhanced field intensity lies, but the limited adsorption capability of some probe molecules makes the hotspots in bare noble metallic structures fail to function fully. 1T′ $MoTe_2$ as a 2D material, on the other hand, allows excellent surface adsorption of probes because of its low-symmetry 1T′ phase and the π-π interaction at the analyte-$MoTe_2$

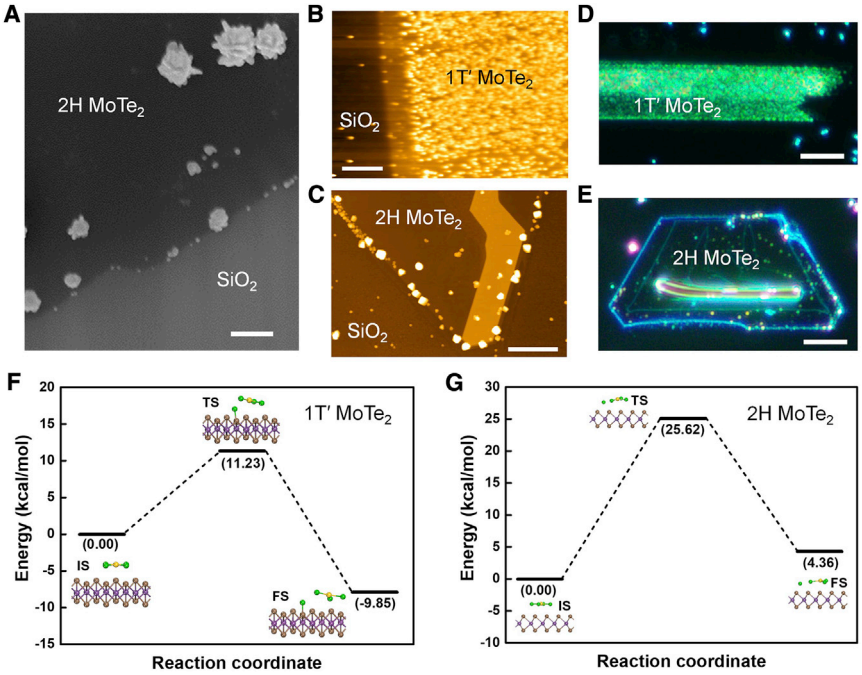

Figure 2. Formation of AuNPs on 1T′ and 2H $MoTe_2$: The phase matters

(A) SEM image of 2H $MoTe_2$ (3L) after $HAuCl_4$ treatment for 30 s. Scale bar, 400 nm.

(B and C) AFM images of 1T′ (B) and 2H (C) $MoTe_2$ after $HAuCl_4$ treatment. Scale bars, 2 μm.

(D and E) Dark-field optical images of 1T′ (D) and 2H (E) $MoTe_2$ after $HAuCl_4$ treatment. Scale bars, 10 μm.

(F and G) The minimum energy pathways, including the initial state (IS), transition state (TS), and final state (FS), for dechlorination of the $[AuCl_4]^-$ ion on 1T′ (F) and 2H (G) $MoTe_2$ surfaces.

interface. As a result, the AuNPs-$MoTe_2$ hybrid delivers a superior platform with increased SERS sensitivity. $MoTe_2$ not only augments the number of analytes adsorbed at hotspot regions but also introduces coupled chemical enhancement. The charge transfer resonances between analytes and $MoTe_2$ are largely promoted by leveraging the nearby molecular transition under resonance conditions via a vibronic coupling process[28] and can be enhanced by the strong electromagnetic field generated by the high-density hotspots between AuNPs. The promising SERS effect of AuNPs-$MoTe_2$ hybrids results from cooperative and coupling effects of plasmon at hotspots, chemical enhancement because of efficient charge transfer, and enriched molecular adsorption (see the illustration in Figure 1G and discussion in Note S1).[29] Figure 1H depicts the electric field distribution of AuNPs on the $MoTe_2$ surface under 532-nm illumination, simulated by the finite difference time domain (FDTD) method. A highly localized electromagnetic field distributes in the nano-gaps between AuNPs and at the touchpoint between AuNPs and the $MoTe_2$ sheet, consistent with the analysis above. The AuNPs-$MoTe_2$ hybrid exhibits an LSPR peak around 530 nm, as shown in the extinction spectrum in Figure S3.

Effect of the $MoTe_2$ phase on AuNP formation

As discussed above, spontaneous *in situ* formation of AuNPs can be realized on 1T′ $MoTe_2$, but it is not applicable to 2H $MoTe_2$ with low surface activity.[30] SEM and AFM images of $MoTe_2$ possessing different phases after $HAuCl_4$ treatment are shown in Figures 1D and 2A–2C. Further, we investigated the morphologies of AuNPs on $MoTe_2$ using a dark-field microscopy technique that enables high-contrast imaging of plasmonic nanoparticles (Figures 2D and 2E).[31] The characterization results show

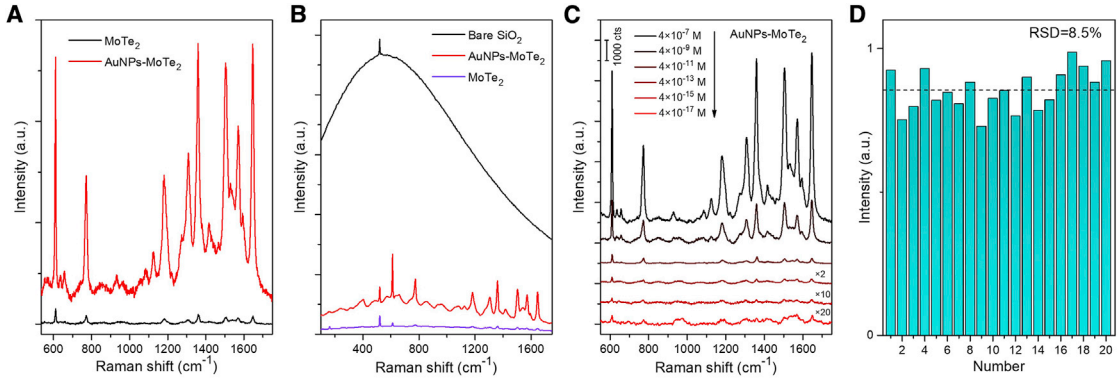

Figure 3. SERS performance and FL quenching

(A) SERS signals of R6G (4×10^{-7} M) on bare $MoTe_2$ and the AuNPs-$MoTe_2$ hybrid structure.

(B) Raman-FL spectra of R6G on bare SiO_2 and $MoTe_2$ and the AuNPs-$MoTe_2$ hybrid structure.

(C) SERS signals collected on AuNPs-$MoTe_2$ with various concentrations of R6G coating.

(D) Histograms of the SERS intensities of the R6G 1,646 cm^{-1} feature peak on the AuNPs-$MoTe_2$ hybrid with R6G coating (4×10^{-7} M). The derived relative standard deviation (RSD) is 8.5%.

that high-density AuNPs are formed on the surface of 1T′ $MoTe_2$, whereas only few large Au aggregates are detected on 2H $MoTe_2$. As shown in Figure S4, $HAuCl_4$ treatment does not result in measurable improvement of the SERS sensitivity of 2H $MoTe_2$. The significant difference between the morphologies of the $HAuCl_4$-treated 1T′ and 2H $MoTe_2$ can be illustrated by density-functional theory (DFT) calculation, as shown in Figures 2F and 2G. The DFT results show that the energy barrier (E_b) for the dechlorinating of $[AuCl_4]^-$ ion on the 1T′ $MoTe_2$ surface is only 11.23 kcal/mol, whereas E_b reaches 25.62 kcal/mol on the 2H $MoTe_2$ surface. Thus, we can draw an intuitive scenario of the reaction rate k for $[AuCl_4]^-$ ion dechlorination on the 1T′ and 2H $MoTe_2$ surface through a simple unimolecular reaction model,[32]

$$k = \frac{k_B T}{h}\left(\frac{RT}{P_0}\right)^{\Delta n} \exp\left(-\frac{E_b}{k_B T}\right), \qquad \text{(Equation 1)}$$

where k_B is the Boltzmann constant, h is the Planck constant, T is the thermodynamic temperature, R is the universal gas constant, and P_0 is the standard atmosphere, and for a unimolecular reaction, $\Delta n = 0$. From Equation 1, it can be obtained that, at room temperature (T = 298.15 K), the half-life of the $[AuCl_4]^-$ ion on the 1T′ $MoTe_2$ surface $t(1/2) = \ln(2/k)$ is much less than 1 s. However, on the 2H $MoTe_2$ surface, the half-life of the $[AuCl_4]^-$ ion is ~190 h. From such a remarkable difference of $[AuCl_4]^-$ ion half-lives on the 1T′ and 2H $MoTe_2$ surface, we can conclude that, on the surface of 1T′ $MoTe_2$, the $[AuCl_4]^-$ ion can be fleetly reduced to AuNPs at room temperature, whereas on the surface of 2H $MoTe_2$, dechlorination of the $[AuCl_4]^-$ ion cannot proceed spontaneously unless on the defective sites. The 1T′ phase possessing high surface activity largely facilitates AuNP formation. Thus, in stark contrast to the 2H counterpart, 1T′ $MoTe_2$ not only has considerably larger CM-based SERS sensitivity[11,33] but also benefits spontaneous formation of plasmonic nanoparticles, making the AuNPs-$MoTe_2$ hybrid an ultrasensitive and easily fabricated platform for SERS with EM-CM coupling.

SERS performance of the hybrid platform

Figure 3A shows a direct comparison of the SERS signals (with baseline correction) of a typical probe, R6G, with a 4×10^{-7} M concentration drop casted on bare 1T′ $MoTe_2$ and AuNPs-$MoTe_2$ hybrid substrates (532-nm excitation). The detected R6G Raman-active peaks on the hybrid structure are much stronger than those on

pure 1T′ $MoTe_2$, although 1T′ $MoTe_2$ has been demonstrated to present a much more sensitive SERS effect than the intensively studied graphene, *h*BN, and MoS_2.[11] We also found that the SERS sensitivity of few-layer WTe_2 as another 1T′ TMT material is much enhanced after $HAuCl_4$ treatment, similar to the case of 1T′ $MoTe_2$ (Figure S5). Additionally, 1T′ $MoTe_2$ acts as a promising analyte FL quencher, delivering clean SERS signals, whereas the large FL background is a major hurdle of resonance SERS on metallic plasmonic substrates.[34,35] As shown in Figure 3B, the SERS outputs on AuNPs-$MoTe_2$ are of high signal-to-background ratio, whereas the signals on bare SiO_2 performs large FL background of R6G with no detectable analyte Raman peaks. The FL quenching effect is a consequence of charge transfer and energy transfer between R6G and $MoTe_2$.[11,25] The formation procedure of dense and self-assembled AuNPs on $MoTe_2$ is simple and efficient within 30 s, and a further increase in immersion time in $HAuCl_4$ solution does not result in more effective SERS performance of the fabricated AuNPs-$MoTe_2$ (Figures S6A and S6B). This is attributed to the aggregation of AuNPs with prolonged reaction time, which decreases the density of hotspots (see SEM images in Figures S6C–S6F).

We also investigated the influence of Raman excitation wavelength on SERS sensitivity. As shown in Figure S7, the dye Raman features exhibit larger enhancement when the excitation is resonant with the probes, under which condition the charge transfer resonance can be maximized. Nevertheless, the dyes coated on AuNPs-$MoTe_2$ show acceptable SERS sensitivities with non-resonance excitation wavelengths because of the incorporation of EM. On the other hand, the SERS effect can be barely observed on substrates based solely on CM when the excitation does not resonate with the probes.[11,36]

By taking advantages of plasmonic localized field enhancement and chemical enhancement, the novel AuNPs-$MoTe_2$ hybrid is expected to detect analytes at ultra-low concentrations. Figure 3C presents the SERS spectra of R6G coated on AuNPs-$MoTe_2$ with various concentrations from 4×10^{-7} to 4×10^{-17} M. Distinct Raman fingerprint peaks of R6G are clearly detected. At an ultra-low R6G concentration of 4×10^{-17} M, the SERS signals are still detectable, giving rise to the capability of detecting trace amount of analytes on the AuNPs-$MoTe_2$. This ideal limit of detection (LoD) is four orders of magnitude improved in comparison with the individual 1T′ $MoTe_2$ substrates[11] and far surpasses the previously reported results of metal nanostructures hybridized with graphene, *h*BN, MoS_2, and other 2D materials, whose fabrication processes are much more complicated, costly, and time consuming.[16,17,37,38] A detailed comparison between the present work and other plasmonic-2D material based SERS substrates is listed in Table S1. The intensity of the R6G 609 cm^{-1} feature peak and concentration of coated R6G shows a linear relationship in log scale (Figure S8), suggesting that the AuNPs-$MoTe_2$ platform is promising for quantitative molecular detection.

The SERS intensities collected on AuNPs-$MoTe_2$ are uniformly distributed, as evidenced by the Raman intensity map of the R6G 609 cm^{-1} peak in Figure S9A. The SiO_2 areas shows no appreciable R6G Raman signals because the AuNPs cannot be formed on bare SiO_2. SERS spectra collected from 20 randomly selected spots on AuNPs-$MoTe_2$ are shown in Figure S9B, and the corresponding histograms of the R6G Raman intensity depicted in Figure 3D reveal a small relative standard deviation of 8.5% in the SERS signals. This high homogeneity of the SERS signals is attributed to the atomic flat surface of the 2D $MoTe_2$, which uniformly adsorbs analytes, and the uniform morphology of the *in situ* self-assembled AuNPs. This feature gives rise to the reproducible and quantitative molecular detection on the hybrid

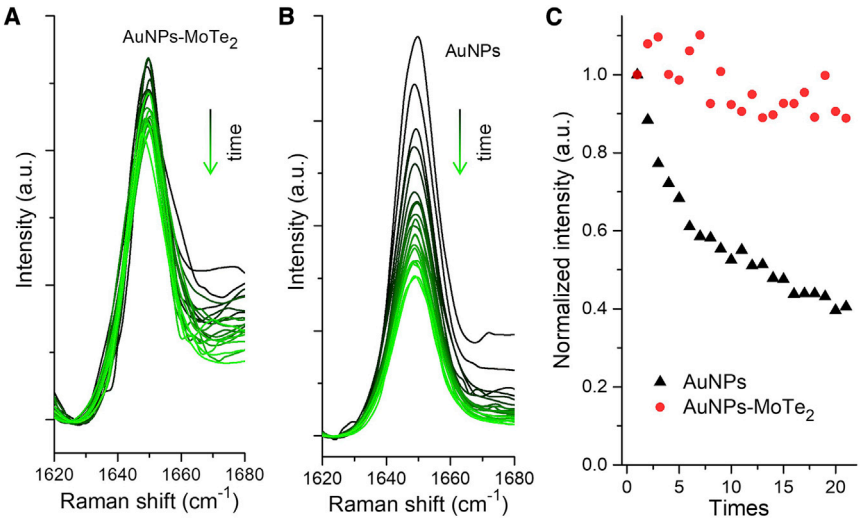

Figure 4. SERS stability under illumination

(A and B) SERS signals of the R6G 1,646 cm^{-1} feature peak on the AuNPs-$MoTe_2$ hybrid structure (A) and bare AuNPs (B) under continuous laser illumination. Each spectrum was collected with 10-s acquisition time and a 10-s interval before the next measurement.

(C) SERS intensities of the R6G 1,646 cm^{-1} peak with increasing numbers of spectral acquisitions.

SERS platform, which is of technical importance in real-world applications. The photobleaching effect of dyes on metallic nanostructures is another factor that leads to low reproducibility in conventional SERS detection. Even for some semiconductor SERS substrates, photocatalytic degradation of the analyte is non-negligible.[39] The AuNPs-$MoTe_2$ hybrid can greatly eliminate the unwanted degradation of probes upon illumination. To conduct a comparative investigation of photostability, a control substrate of AuNPs on SiO_2/Si was fabricated by depositing 10-nm gold film on SiO_2, followed by vacuum annealing at 300°C. As shown in Figure 4, the R6G Raman intensities on AuNPs-$MoTe_2$ remain mostly stable with prolonged laser illumination, whereas those on the conventional substrate (AuNPs) present a significant decrease with increasing acquisition time. The highly improved stability against illumination on AuNPs-$MoTe_2$ can be attributed to the large charge transfer between the analytes and $MoTe_2$, which promotes relaxation of analyte excitation states and dissipation of hot electrons.[40]

The AuNPs-$MoTe_2$ hybrid structure is suitable for various analytical applications, such as detecting risky chemicals in food. We tested trace amounts of the Sudan III and crystal violet (CV) dyes on the hybrid SERS platform, which are a category 3 carcinogen classified by IARC and a harmful fish drug, respectively. The SERS signals of Sudan III and CV coated on AuNPs-$MoTe_2$ are plotted in Figures S10A and S10B. The analyte fingerprint peaks are clearly detected, even at an ultra-low analyte concentration of 4×10^{-15} M, showing the potential of the AuNPs-$MoTe_2$ hybrid for food safety and environmental pollution monitoring with high sensitivity. The feature peak intensities of the analytes as functions of the analyte concentrations are given in Figures S10C and S10D.

Flexible SERS tapes for real-world applications

To realize real-time, *in situ* and reliable SERS detection for daily life applications, we fabricated flexible and transparent SERS tapes based on AuNPs-$MoTe_2$ that can be applied on arbitrary surfaces. As shown in Figure 5A, a large-area continuous thin

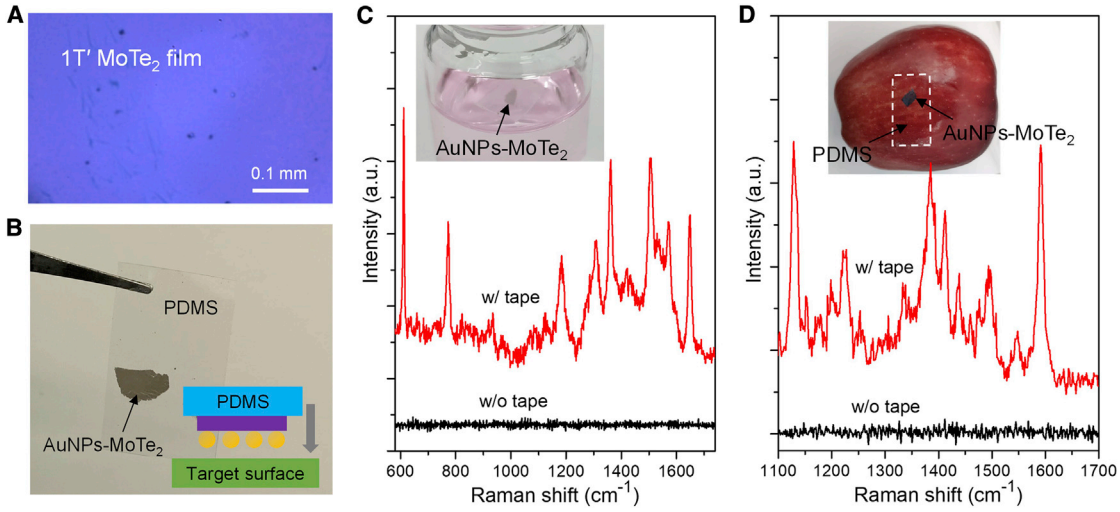

Figure 5. Flexible SERS tape for practical applications

(A) Optical image of the large-area continuous thin film of 1T′ $MoTe_2$.

(B) Image of the flexible AuNP/$MoTe_2$/PDMS SERS tape. Inset: a schematic showing that the SERS tape can be applied to target surfaces for various applications.

(C) SERS detection with and without SERS tape floating on the R6G aqueous solution.

(D) SERS detection with and without SERS tape stuck on the apple surface with adsorbed Sudan III dye.

film of 1T′ $MoTe_2$ was synthesized on SiO_2/Si by tellurization of a 2-nm pre-deposited Mo film (the Raman spectrum and intensity map in Figure S11 show the high quality and uniformity of the $MoTe_2$ film).[41] The $MoTe_2$ film was then transferred onto a polydimethylsiloxane (PDMS) stamp, and the AuNP/$MoTe_2$/PDMS SERS tape was obtained after $HAuCl_4$ treatment (Figure 5B). The fabrication process of the SERS tape is detailed in the Experimental procedures. Here we show two typical application scenarios. As shown in Figure 5C, the SERS tape can float on an aqueous solution of analyte (10^{-6} M R6G was used as an example), and the analyte Raman signals can be clearly detected with the SERS tape. Figure 5D shows another application where the SERS tape sticks to an apple surface. The apple was immersed in Sudan III solution (10^{-6} M) for 20 min before adhesion of the SERS tape. Distinct Raman signals from the analyte molecules adsorbed on the apple surface are observed *in situ* on the SERS tape-covered area, whereas no analyte signal is collected on the area without SERS tape. The detection sensitivity of the SERS tape is expected to be improved by optimizing the growth process used to obtain the $MoTe_2$ continuous film with higher crystallinity because grain boundaries would impede the charge transfer.

DISCUSSION

We demonstrated that uniform and high-density AuNPs can be prepared *in situ* on 2D 1T′ $MoTe_2$ via facile and fast chemical treatment without design constraints, spontaneously forming a hybrid structure for SERS. The high surface activity of the 1T′ phase is not only crucial for formation of AuNPs but also leads to a strongly interacting analyte-$MoTe_2$ interface. The AuNPs-$MoTe_2$ SERS platform generates coupling effects of plasmonic enhancement and chemical enhancement, providing ultrasensitive molecular detection. Additionally, the hybrid structure delivers uniform, reproducible, and clean SERS signals, and the SERS signal intensities remain stable under prolonged laser illumination. Our work demonstrates that the easily fabricated hybrid SERS substrate is promising for practical applications such as

food safety control and enhances our understanding of electromagnetic and chemical enhancements of SERS.

EXPERIMENTAL PROCEDURES

Resource availability

Lead contact

Requests for further information and resources should be directed to and will be fulfilled by the lead contact, Li Tao (taoli@link.cuhk.edu.hk).

Materials availability

This study did not generate new unique reagents.

Data and code availability

All of the data associated with this study are included in the article and Supplemental information. Additional information is available from the lead contact upon reasonable request.

Material growth and characterization

$MoTe_2$ atomic layers were synthesized in a home-built CVD system using a space-confined strategy.[42] 20 mg ammonium molybdate tetrahydrate was placed in a quartz boat as the precursor. 2 mg NaCl was added to the same boat as the growth promoter.[43] SiO_2/Si substrate cleaned with acetone sonication was put on the boat with a face-to-face configuration. Another boat containing 50 mg tellurium powder was placed in the upstream region of the CVD chamber close to the growth substrate (1 cm). Growth was conducted at atmospheric pressure with an Ar/H_2 (250/20 sccm) carrier gas environment. The furnace was heated to 810°C in 15 min and kept for 10 min for growth of 1T′ $MoTe_2$. The growth temperature was decreased to 650°C to produce 2H $MoTe_2$. In the main text, the $MoTe_2$ is of 1T′ phase unless specified otherwise. SEM images were obtained by SUPRA 60 with 10-kV accelerating voltage, and TEM images were taken by a Titan3 G2 60-300 (FEI). AFM (NTEGRA, NT-MDT) was used to characterize the surface morphology. XPS measurements were conducted by ESCALAB 250Xi. Raman/FL spectra were acquired with a Horiba LabRAM HR Evolution Raman system using 532-nm excitation unless specified otherwise.

FDTD simulation

A commercial FDTD simulation package (FDTD Solutions, Lumerical) was used with 3D simulation for calculating the near field profile and scattering/absorption spectrum of the AuNPs/1T′ $MoTe_2$ hybrid structure. Two AuNPs with a diameter of 20 nm and a gap of 3 nm were set on 1T′ $MoTe_2$ with a thickness of 3 nm; the structure was on the SiO_2 substrate, and the simulation background was air. A normal incident total field-scattering field (TFSF) source was used with polarization along the line of the two nanospheres centers. The antisymmetric and symmetric boundary conditions were used accordingly for reducing the simulation time and resource requirements; the others were set to be perfectly matched layers. The mesh sizes for the regions of the two nanospheres and 1T′ $MoTe_2$ were set to be 0.5 and 0.25 nm, respectively. Two optical power analysis groups inside and outside of the TFSF source region were used for calculating the absorption and scattering spectrum.

DFT calculation

DFT calculations were performed using the Perdew-Burke-Ernzerhof (PBE) functional within the generalized gradient approximation (GGA) used to describe the exchange-correlation interactions. Projector-augmented wave (PAW) pseudopotentials were used to describe the core electrons. All calculations were done using

VASP code.[44] The wave functions were expanded in plane waves up to a cutoff of 400 eV. The Brillouin zone integration was sampled by a 2 × 2 × 1 k mesh. The systems were simulated with a periodic boundary condition by placing a $[AuCl_4]^-$ ion on the surface of 72-atom 1T′ $MoTe_2$ (Mo:24 and Te:48) and 75-atom 2H $MoTe_2$ (Mo:25 and Te:50), respectively. We performed full geometry optimizations until the residual forces were less than 0.01 eV/Å. To compute the reaction barriers, we used the NEB method with the 'climbing image' algorithm.[45] Activation barriers obtained with the NEB method refer to a temperature of 0 K. The reaction pathway by means of NEB calculations was based on the constrained geometry optimizations. Therefore, all intermediate states were identified by a series of constrained geometry optimizations. After a constraint is defined (e.g., the forces between atoms), geometry optimization is performed to force the constraint to preserve a given value.

SERS measurements

A sequential dilution process was performed for obtaining an aqueous solution of the analytes (R6G, CV, and Sudan III) with various concentrations. The SERS substrates were immersed in the analyte solution for 20 min to coat the analyte molecules. SERS spectra were collected using a Horiba LabRAM HR Evolution Raman system with a 532-nm excitation laser (unless specified otherwise) and 100× objective lens. The laser spot size was around 1 μm. For each spectral acquisition, the laser power was 3.2 mW, and the integration time was 2 s (unless specified otherwise). For SERS measurements with an analyte concentration lower than 10^{-14} M, the signal intensities were averaged from five individual acquisitions to enhance the signal-to-noise ratio. Baseline correction was performed in the SERS spectra, expect for the Raman-FL spectra in Figure 3B.

Flexible SERS tape fabrication

Mo film of 2-nm thickness was deposited on SiO_2/Si substrate via electron beam evaporation. The Mo film was then tellurized into a 1T′ $MoTe_2$ continuous film in the CVD furnace at 810°C. After growth, the SiO_2 substrate was etched in HF aqueous solution (10%), and the 1T′ $MoTe_2$ film was then transferred onto a PDMS film (Gel-Pak). A supporting polymer, such as poly(methyl methacrylate), was not applied during the transfer because the 1T′ $MoTe_2$ film is of excellent robustness. After gentle drying and baking (80°C for 10 min), the $MoTe_2$/PDMS stack was immersed in $HAuCl_4$ solution (1 mM) for 30 s for formation of dense AuNPs on the $MoTe_2$ surface. Then the fabricated AuNP/$MoTe_2$/PDMS flexible SERS tape was ready for application to target surfaces for various applications.

SUPPLEMENTAL INFORMATION

Supplemental information can be found online at https://doi.org/10.1016/j.xcrp.2021.100526.

ACKNOWLEDGMENTS

The work is supported in part by the Research Grants Council of Hong Kong (AoE/P-02/12); the CUHK Group Research Scheme; ITS/390/18 and Research Talent Hub Scheme for the ITF project by the Innovation and Technology Commission, Hong Kong SAR Government; the National Natural Science Foundation of China (62005051, 51802360, 61975036, and 61804067), the National Natural Science Foundation of Guangdong for Distinguished Young Scholars (2018B030306043), the Pearl River Talent Plan (2019QN01C109), the Science and Technology Program of Guangzhou (201904010449), and the Key Cultivation Program for Young Teachers of Sun Yat-sen University (20lgzd13).

AUTHOR CONTRIBUTIONS

L.T. conceived the project with supervision from J.B.X. and K.C. L.T. and K.C. synthesized and characterized the materials with assistance from Y. Zhou, H.L., X. Wang, and R.Z. L.T. performed the Raman experiments with assistance from K.C., X.H., and Y. Zhao. K.C. and Z.L. conducted the theoretical modeling and calculations. L.T., K.C., and J.B.X. wrote the paper. All authors discussed the results and commented on the manuscript.

DECLARATION OF INTERESTS

The authors declare no competing interests.

Received: April 9, 2021
Revised: June 11, 2021
Accepted: July 14, 2021
Published: August 2, 2021

REFERENCES

1. Sharma, B., Frontiera, R.R., Henry, A.-I., Ringe, E., and Van Duyne, R.P. (2012). SERS: Materials, applications, and the future. Mater. Today *15*, 16–25.
2. Schlücker, S. (2014). Surface-enhanced Raman spectroscopy: concepts and chemical applications. Angew. Chem. Int. Ed. Engl. *53*, 4756–4795.
3. Gaufrès, E., Tang, N.Y.W., Lapointe, F., Cabana, J., Nadon, M.-A., Cottenye, N., Raymond, F., Szkopek, T., and Martel, R. (2014). Giant Raman scattering from J-aggregated dyes inside carbon nanotubes for multispectral imaging. Nat. Photonics *8*, 72–78.
4. Kitadai, H., Wang, X., Mao, N., Huang, S., and Ling, X. (2019). Enhanced Raman Scattering on Nine 2D van der Waals Materials. J. Phys. Chem. Lett. *10*, 3043–3050.
5. Ling, X., Xie, L., Fang, Y., Xu, H., Zhang, H., Kong, J., Dresselhaus, M.S., Zhang, J., and Liu, Z. (2010). Can graphene be used as a substrate for Raman enhancement? Nano Lett. *10*, 553–561.
6. Ling, X., Fang, W., Lee, Y.-H.H., Araujo, P.T., Zhang, X., Rodriguez-Nieva, J.F., Lin, Y., Zhang, J., Kong, J., and Dresselhaus, M.S. (2014). Raman enhancement effect on two-dimensional layered materials: graphene, h-BN and MoS2. Nano Lett. *14*, 3033–3040.
7. Muehlethaler, C., Considine, C.R., Menon, V., Lin, W.-C., Lee, Y.-H., and Lombardi, J.R. (2016). Ultrahigh Raman Enhancement on Monolayer MoS2. ACS Photonics *3*, 1164–1169.
8. Lombardi, J.R., and Birke, R.L. (2008). A Unified Approach to Surface-Enhanced Raman Spectroscopy. J. Phys. Chem. C *112*, 5605–5617.
9. Wang, X., and Guo, L. (2020). SERS Activity of Semiconductors: Crystalline and Amorphous Nanomaterials. Angew. Chem. Int. Ed. Engl. *59*, 4231–4239.
10. Song, G., Gong, W., Cong, S., and Zhao, Z. (2021). Ultrathin Two-Dimensional Nanostructures: Surface Defects for Morphology-Driven Enhanced Semiconductor SERS. Angew. Chem. Int. Ed. Engl. *60*, 5505–5511.
11. Tao, L., Chen, K., Chen, Z., Cong, C., Qiu, C., Chen, J., Wang, X., Chen, H., Yu, T., Xie, W., et al. (2018). 1T′ Transition Metal Telluride Atomic Layers for Plasmon-Free SERS at Femtomolar Levels. J. Am. Chem. Soc. *140*, 8696–8704.
12. Song, X., Wang, Y., Zhao, F., Li, Q., Ta, H.Q., Rümmeli, M.H., Tully, C.G., Li, Z., Yin, W.-J., Yang, L., et al. (2019). Plasmon-Free Surface-Enhanced Raman Spectroscopy Using Metallic 2D Materials. ACS Nano *13*, 8312–8319.
13. Seo, J., Lee, J., Kim, Y., Koo, D., Lee, G., and Park, H. (2020). Ultrasensitive Plasmon-Free Surface-Enhanced Raman Spectroscopy with Femtomolar Detection Limit from 2D van der Waals Heterostructure. Nano Lett. *20*, 1620–1630.
14. Tao, L., Chen, Z., Li, Z., Wang, J., Xu, X., and Xu, J.-B. (2021). Enhancing light-matter interaction in 2D materials by optical micro/nano architectures for high-performance optoelectronic devices. InfoMat *3*, 36–60.
15. Xu, W., Ling, X., Xiao, J., Dresselhaus, M.S., Kong, J., Xu, H., Liu, Z., and Zhang, J. (2012). Surface enhanced Raman spectroscopy on a flat graphene surface. Proc. Natl. Acad. Sci. USA *109*, 9281–9286.
16. Xu, W., Xiao, J., Chen, Y., Chen, Y., Ling, X., and Zhang, J. (2013). Graphene-veiled gold substrate for surface-enhanced Raman spectroscopy. Adv. Mater. *25*, 928–933.
17. Cai, Q., Mateti, S., Yang, W., Jones, R., Watanabe, K., Taniguchi, T., Huang, S., Chen, Y., and Li, L.H. (2016). Boron Nitride Nanosheets Improve Sensitivity and Reusability of Surface-Enhanced Raman Spectroscopy. Angew. Chem. Int. Ed. Engl. *55*, 8405–8409.
18. Cai, Q., Mateti, S., Watanabe, K., Taniguchi, T., Huang, S., Chen, Y., and Li, L.H. (2016). Boron Nitride Nanosheet-Veiled Gold Nanoparticles for Surface-Enhanced Raman Scattering. ACS Appl. Mater. Interfaces *8*, 15630–15636.
19. Lu, R., Konzelmann, A., Xu, F., Gong, Y., Liu, J., Liu, Q., Xin, M., Hui, R., and Wu, J.Z. (2015). High sensitivity surface enhanced Raman spectroscopy of R6G on in situ fabricated Au nanoparticle/graphene plasmonic substrates. Carbon N. Y. *86*, 78–85.
20. Yang, L., Lee, J.-H., Rathnam, C., Hou, Y., Choi, J.-W., and Lee, K.-B. (2019). Dual-Enhanced Raman Scattering-Based Characterization of Stem Cell Differentiation Using Graphene-Plasmonic Hybrid Nanoarray. Nano Lett. *19*, 8138–8148.
21. Wang, Y., Ni, Z., Hu, H., Hao, Y., Wong, C.P., Yu, T., Thong, J.T.L., and Shen, Z.X. (2010). Gold on graphene as a substrate for surface enhanced Raman scattering study. Appl. Phys. Lett. *97*, 163111.
22. Liu, Y., Guo, J., Zhu, E., Liao, L., Lee, S.J., Ding, M., Shakir, I., Gambin, V., Huang, Y., and Duan, X. (2018). Approaching the Schottky-Mott limit in van der Waals metal-semiconductor junctions. Nature *557*, 696–700.
23. Seok, J., Lee, J.-H., Cho, S., Ji, B., Kim, H.W., Kwon, M., Kim, D., Kim, Y.-M., Oh, S.H., Kim, S.W., et al. (2017). Active hydrogen evolution through lattice distortion in metallic MoTe2. 2D Mater. *4*, 025061.
24. McGlynn, J.C., Dankwort, T., Kienle, L., Bandeira, N.A.G., Fraser, J.P., Gibson, E.K., Cascallana-Matías, I., Kamarás, K., Symes, M.D., Miras, H.N., and Ganin, A.Y. (2019). The rapid electrochemical activation of $MoTe_2$ for the hydrogen evolution reaction. Nat. Commun. *10*, 4916.
25. Chen, P., Yin, Z., Huang, X., Wu, S., Liedberg, B., and Zhang, H. (2011). Assembly of Graphene Oxide and Au0.7Ag0.3 Alloy Nanoparticles on SiO2 : A New Raman Substrate with Ultrahigh Signal-to-Background Ratio. J. Phys. Chem. C *115*, 24080–24084.
26. Shi, Y., Wang, J., Wang, C., Zhai, T.-T., Bao, W.-J., Xu, J.-J., Xia, X.-H., and Chen, H.-Y. (2015). Hot electron of Au nanorods activates the electrocatalysis of hydrogen evolution on MoS2 nanosheets. J. Am. Chem. Soc. *137*, 7365–7370.

27. Lu, J., Lu, J.H., Liu, H., Liu, B., Gong, L., Tok, E.S., Loh, K.P., and Sow, C.H. (2015). Microlandscaping of Au nanoparticles on few-layer MoS2 films for chemical sensing. Small *11*, 1792–1800.

28. Lombardi, J.R., Birke, R.L., Lu, T., and Xu, J. (1986). Charge-transfer theory of surface enhanced Raman spectroscopy: Herzberg–Teller contributions. J. Chem. Phys. *84*, 4174–4180.

29. Lombardi, J.R. (2017). The theory of surface-enhanced Raman scattering on semiconductor nanoparticles; toward the optimization of SERS sensors. Faraday Discuss. *205*, 105–120.

30. Lukowski, M.A., Daniel, A.S., Meng, F., Forticaux, A., Li, L., and Jin, S. (2013). Enhanced hydrogen evolution catalysis from chemically exfoliated metallic MoS2 nanosheets. J. Am. Chem. Soc. *135*, 10274–10277.

31. Liu, M., Chao, J., Deng, S., Wang, K., Li, K., and Fan, C. (2014). Dark-field microscopy in imaging of plasmon resonant nanoparticles. Colloids Surf. B Biointerfaces *124*, 111–117.

32. Fernández-Ramos, A., Ellingson, B.A., Meana-Pañeda, R., Marques, J.M.C., and Truhlar, D.G. (2007). Symmetry numbers and chemical reaction rates. Theor. Chem. Acc. *118*, 813–826.

33. Fraser, J.P., Masaityte, L., Zhang, J., Laing, S., Moreno-López, J.C., McKenzie, A.F., McGlynn, J.C., Panchal, V., Graham, D., Kazakova, O., et al. (2020). Selective phase growth and precise-layer control in MoTe2. Commun. Mater. *1*, 48.

34. Xie, L., Ling, X., Fang, Y., Zhang, J., and Liu, Z. (2009). Graphene as a substrate to suppress fluorescence in resonance Raman spectroscopy. J. Am. Chem. Soc. *131*, 9890–9891.

35. Shim, S., Stuart, C.M., and Mathies, R.A. (2008). Resonance Raman cross-sections and vibronic analysis of rhodamine 6G from broadband stimulated Raman spectroscopy. ChemPhysChem *9*, 697–699.

36. Feng, S., Dos Santos, M.C., Carvalho, B.R., Lv, R., Li, Q., Fujisawa, K., Elías, A.L., Lei, Y., Perea-López, N., Endo, M., et al. (2016). Ultrasensitive molecular sensor using N-doped graphene through enhanced Raman scattering. Sci. Adv. *2*, e1600322.

37. Meng, X., Wang, H., Chen, N., Ding, P., Shi, H., Zhai, X., Su, Y., and He, Y. (2018). A Graphene-Silver Nanoparticle-Silicon Sandwich SERS Chip for Quantitative Detection of Molecules and Capture, Discrimination, and Inactivation of Bacteria. Anal. Chem. *90*, 5646–5653.

38. Li, Z., Jiang, S., Huo, Y., Liu, A., Zhang, C., Yu, J., Wang, M., Li, C., Lu, Z., and Man, B. (2018). 3D Hybrid Plasmonic Nanostructures with Dense Hot Spots Using Monolayer MoS2 as Sub-Nanometer Spacer. Adv. Mater. Interfaces *5*, 1800661.

39. Yang, L., Peng, Y., Yang, Y., Liu, J., Huang, H., Yu, B., Zhao, J., Lu, Y., Huang, Z., Li, Z., and Lombardi, J.R. (2019). A Novel Ultra-Sensitive Semiconductor SERS Substrate Boosted by the Coupled Resonance Effect. Adv. Sci. (Weinh.) *6*, 1900310.

40. Zhao, Y., Xie, Y., Bao, Z., Tsang, Y.H., Xie, L., and Chai, Y. (2014). Enhanced SERS Stability of R6G Molecules with Monolayer Graphene. J. Phys. Chem. C *118*, 11827–11832.

41. Zhou, L., Xu, K., Zubair, A., Liao, A.D., Fang, W., Ouyang, F., Lee, Y.-H., Ueno, K., Saito, R., Palacios, T., et al. (2015). Large-Area Synthesis of High-Quality Uniform Few-Layer MoTe2. J. Am. Chem. Soc. *137*, 11892–11895.

42. Tao, L., Chen, K., Chen, Z., Chen, W., Gui, X., Chen, H., Li, X., and Xu, J.-B. (2017). Centimeter-Scale CVD Growth of Highly Crystalline Single-Layer MoS_2 Film with Spatial Homogeneity and the Visualization of Grain Boundaries. ACS Appl. Mater. Interfaces *9*, 12073–12081.

43. Zhou, J., Lin, J., Huang, X., Zhou, Y., Chen, Y., Xia, J., Wang, H., Xie, Y., Yu, H., Lei, J., et al. (2018). A library of atomically thin metal chalcogenides. Nature *556*, 355–359.

44. Kresse, G., and Furthmüller, J. (1996). Efficient iterative schemes for ab initio total-energy calculations using a plane-wave basis set. Phys. Rev. B Condens. Matter *54*, 11169–11186.

45. Henkelman, G., Uberuaga, B.P., and Jónsson, H. (2000). A climbing image nudged elastic band method for finding saddle points and minimum energy paths. J. Chem. Phys. *113*, 9901–9904.